AGU PUBLICATIONS

JGR

Journal of Geophysical Research: Oceans

RESEARCH ARTICLE

10.1002/2015JC011200

A laboratory study of spilling breakers in the presence of light-wind and surfactants

Xinan Liu[1]

[1]Department of Mechanical Engineering, University of Maryland, College Park, Maryland, USA

Key Points:
- Breaking waves in the presence of light-wind and surfactants are studied experimentally
- The bulge-capillary-waves pattern is independent of wind, but markedly affected by surfactants
- The bulge size on the wave forward face is linearly proportional to the surface wind drift

Correspondence to:
X. Liu,
xliu@umd.edu

Citation:
Liu, X. (2016), A laboratory study of spilling breakers in the presence of light-wind and surfactants, *J. Geophys. Res. Oceans*, *121*, doi:10.1002/2015JC011200.

Received 4 AUG 2015
Accepted 15 FEB 2016
Accepted article online 24 FEB 2016

Abstract Spilling breaking waves in the presence of light-wind and surfactants are studied experimentally in a wind-wave tank. The breaking waves are mechanically generated with a single wave maker motion that produces a weak spilling breaker in clean water without wind. Separate experiments are performed with the same wave maker motion at different low wind speeds in clean water and in water with various concentrations of Triton X-100 (soluble surfactant). The crest profiles of the waves along the center plane of the tank are measured with a laser-induced fluorescence (LIF) technique that utilizes a high-speed camera. In clean water with wind speeds lower than 2.3 m/s (the minimum wind speed of wind-generated waves for clean water in our tank), the breaking of the waves is initiated with a similar bulge-capillary-waves pattern on the forward face of the wave crest as reported in Duncan et al. (1999). When the wind speed is above 3 m/s, wind waves are generated. The wind waves strongly affect the breaking process of the mechanically generated waves. It is found that the bulge-capillary-waves pattern is independent of the wind, but is dramatically affected by surfactants. The slope of the back face of the wave crest decreases with increasing wind speed. At the moment of incipient breaking, the distances between the leading edge of the bulge (called the toe) and the highest point of the wave crest in all cases are linearly proportional to the surface wind drift. After the fluid in the bulge slides down the front face of the wave, the maximum horizontal distance of the toe away from the crest increases as the wind speed increases.

1. Introduction

Both experiments and numerical calculations have shown that the characteristics of short-wavelength weak spilling breaking waves in clean water are dominated by surface tension, see *Ebuchi et al*. [1987], *Duncan et al*. [1994a, 1994b, 1999], *Longuet-Higgins* [1992, 1996, 1997], *Yao et al*. [1996], *Tulin* [1996], *Longuet-Higgins and Dommermuth* [1997], *Fedorov et al*. [1998], *Ceniceros and Hou* [1999], *Tsai and Hung* [2007], and the review by *Duncan* [2001]. In the early stages of these breaking events, a bulge forms on the forward face of the crest and capillary waves appear upstream of the leading edge (called the toe) of the bulge [see *Liu and Duncan*, 2006, Figure 1]. Particle-image velocimetry measurements [*Qiao and Duncan*, 2001] indicate that the transition to turbulence occurs when the flow separates as it attempts to negotiate the highly curved free surface at the toe. Subsequent to the initial separation, the fluid in the bulge appears to slide down the front face of the wave, creating a near-surface shear layer [*Okuda*, 1982; *Lin and Rockwell*, 1994, 1995; *Coakley*, 1997; *Dabiri and Gharib*, 1997; *Qiao and Duncan*, 2001] that contributes to the generation of ripples on the crest [*Longuet-Higgins*, 1994]. These ripples initially move at the speed of the crest but quickly slow down and are left behind the crest.

The water surfaces in nature are typically contaminated by surfactant films that reduce the surface tension and create surface elasticity and viscosity. Through a numerical simulation of the Navier-Stokes equations and the surface advection-diffusion equation of surfactants, *Ceniceros* [2003] found that surfactants accumulate in the crest region of the weak spilling breakers when the diffusion of surfactant on the water surface is weak. The size of the bulge and the amplitude and wavelength of capillary waves mentioned above are greatly reduced in the presence of surfactants. Similar results were obtained by *Liu and Duncan* [2006] in an experimental study of the effects of surfactants on mechanically generated spilling breakers. *Liu and Duncan* [2006] also showed that at moderate surfactant concentrations, some geometrical characteristics of the bulge-capillary-ripples pattern scale with the viscoelastic properties of the surface. At surfactant conditions above the Critical Micelle Concentration (CMC), the wave behaves qualitatively and quantitatively as if it was breaking in a pure liquid with the low surface tension of the surfactant solution [*Liu and Duncan*, 2007].

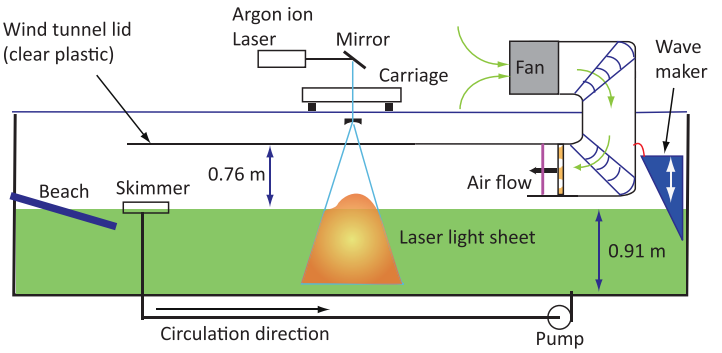

Figure 1. Schematic showing the tank, wave maker, wind tunnel, light sheet, and carriage.

Under some specific surfactant conditions, the wave breaking is initiated with a formation of a small plunging jet that issued from the front face of the wave at a point below the wave crest. The jet projects forward entrapping a pocket of air upon impact with the front face of the wave [*Liu and Duncan*, 2003].

The effect of wind on the breaking of mechanically generated waves has been rarely studied. *Kharif et al*. [2008] experimentally and numerically investigated the influence of strong winds on extreme wave events that were generated by a group of short waves due to the dispersive focusing of a longer frequency-modulated wave train. They found that the wind shifts the focusing point downstream and increases the time duration of the extreme waves. Laboratory studies of the effects of wind on the breaking of shoaling waves were given by *Douglass* [1990] and *King and Baker* [1996], who showed that offshore winds delay the moment of breaking and cause plunging waves whereas onshore winds induce early spilling breakers.

When wind blows over a wave surface, a thin surface drift layer is produced [*Wu*, 1975; *Siddiqui and Loewen*, 2007]. A direct numerical simulation of air turbulence flowing over waves given by *Yang and Shen* [2010] shows that instantaneous air flow separations happen intermittently around the lee side and the trough of the surface wave. They found that the surface wind drift can cause a phase shift of the air turbulence intensity in the downstream direction. The surface wind drift affects wave breaking by changing the occurrence of a stagnation point in a frame of reference moving with the wave [*Banner and Phillips*, 1974; *Phillips and Banner*, 1974]. The wind also produces a temporal and spatial variation of stress distribution along the wave surface. A laboratory measurement given by *Okuda et al*. [1977] showed that skin friction increases continuously at the windward wave surface toward the crest and decreases suddenly just past the crest. The detailed structure of the aqueous surface sublayer flow immediately adjacent to the wind-driven air-water interface has been experimentally investigated by *Banner and Peirson* [1998]. They found that prior to the formation of wind waves, the tangential stress contributes the entire wind stress. As the wave field develops, the mean tangental stress decreases slowly with increasing wind speed while the total wind stress increases significantly. The wind stress may be reduced by surfactants as much as 20–30% because of the reduction of short wind waves [*Uz et al*., 2002].

In this paper, the dynamics of spilling breakers occurring in the presence of both light-wind and ambient surfactants were studied experimentally. Experiments were performed in a tank of clean water and water that was mixed with a soluble surfactant (Triton X-100) at various bulk concentrations. Spilling breakers were generated mechanically with a dispersive focusing technique. The crest-profile histories of the breakers were measured using a photographic technique that employs a laser light sheet, fluorescent dye, and a high-speed movie camera. The geometric characteristics of the crest profiles were correlated with the wind and surface dynamical properties to gain insight into the combined effects of wind and surfactants on the breaking process.

The remainder of this paper is organized as follows. The experimental setup and measurement techniques are described in section 2. The results of the wave measurements are presented in section 3 and discussed in section 4. Finally, the conclusions are given in section 5.

2. Experiment Details

2.1. Wind-Wave Tank

The experiments were performed in a wind-wave tank that is 12 m long, 1.22 m wide, and 2.1 m deep with a water depth of 0.91 m (Figure 1). Waves were generated mechanically with a vertically oscillating wedge located at one end of the tank. The motion of the wedge was controlled by a computer using a position

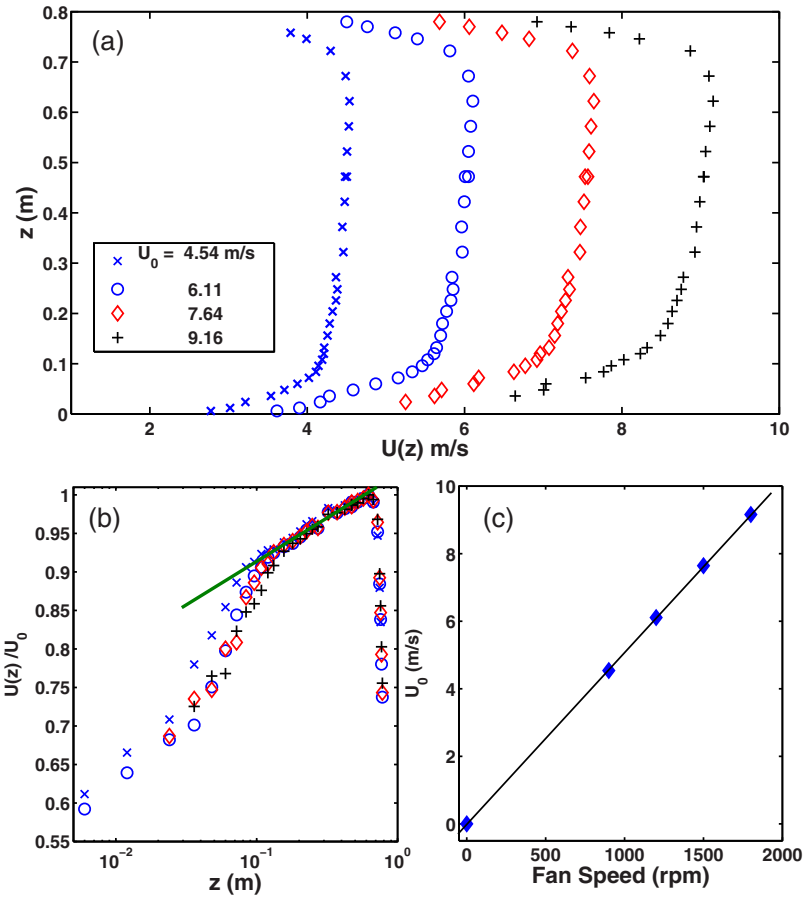

Figure 2. (a) The vertical wind profiles with four fan speeds in the wind tunnel at the location of wave measurements, (b) the vertical wind profiles with four fan speeds after scaled by its own maximum value (U_0), and (c) the maximum wind speed (U_0) versus the fan speed.

sensor in a feedback control loop. The wave reflections at the opposite end of the tank from the wave maker were damped by a tilted beach that is covered with 10.2 cm. thick porous horse hair mats. A wind tunnel above the water surface is formed by the side walls of the tank and a clear Acrylic ceiling positioned 0.78 m above the mean water level. The wind-tunnel ceiling ends about 1 m before the end of the tank to allow the air to exit. The air flow in the tunnel was driven by two 5.6 kW fans that are mounted to the ceiling of the laboratory. An entrance section that consists of two sets of turning vanes, three screens, and a honeycomb is positioned in front of the wave maker to condition and direct the air flow away from the wave maker. The bottom of the entrance section of the wind tunnel is 10.2 cm above the mean water level. This gap allows waves generated by the wave maker to enter the tank. The area between the wave maker and the back of the wind tunnel is sealed with flexible material in order to minimize reverse air flow under the entrance section. Further details about the wave maker and wind tunnel can be found in *Duncan et al*. [1999], *Liu and Duncan* [2006], and *Diorio et al*. [2009].

Prior to the wave measurement, the mean wind velocity profile in the wind tunnel ($U(z)$, where z is the vertical distance from the mean water level) was measured with a Pitot tube as baseline data. The Pitot tube was mounted on a vertical traverser and positioned in the vertical center plane of the tank in the middle of the stream-wise location where the waves broke. The wind profile measurements were performed with the wave maker turned off. A differential pressure transducer (Type 120, MKS, Inc.) was connected to the Pitot tube. The signal from the transducer was recorded on a 16 bit analog-to-digital conversion system (National Instruments, Inc.). Figure 2a shows plots of U versus z for each of four fan speeds. As can be seen from the figure, all the wind profiles are similar to each other and the maximum wind speed (U_0) in each profile was found at $z \approx 0.65$ m for all four cases. The mean wind velocity profiles scaled by their own maximum wind speeds are given in Figure 2b and all data points fall in one curve which forms a linear-logarithmic profile.

The wind profiles at heights between approximate 0.1 and 0.65 m can be fitted with a logarithmic function as follows

$$U(z)/U_0 = K \ln z + D, \tag{1}$$

where $K = 0.0527$ is the slope of the straight line in Figure 2b and D is a constant related to the surface roughness (z_0). Using the logarithmic law $U(z) = \frac{u_*}{\kappa} \ln\left(\frac{z}{z_0}\right)$ with the Von Karman constant $\kappa = 0.41$ yields the wind friction velocity

$$u_* = 0.0216 U_0. \tag{2}$$

Equation (2) shows that the wind friction velocity is about 2.16% of the maximum wind speed in the tank. A plot of the maximum wind speed (U_0) in the wind velocity profile against the fan speed is given in Figure 2c, showing a linear relationship between the two variables. In the remainder of this paper, the wind speed for each experimental condition is denoted by U_0, though the fan speed was recorded.

2.2. Wave Generation and Measurement

Waves were mechanically generated with a dispersive focusing technique [*Longuet-Higgins*, 1974; *Rapp and Melville*, 1990]. The wave-maker-motion parameters were identical to those described in *Duncan et al.* [1999]. The waves broke at a fetch about 4.0 m in the wind tunnel. Only one wave-maker motion with an average wave packet frequency $f_0 = 1.15$ Hz and a nondimensional wave amplitude, $A/\lambda_0 = 0.0505$ (where A is the overall amplitude and $\lambda_0 = g/(2\pi f_0^2)$ is the wavelength of the average frequency according to linear wave theory) was used in this study.

The profiles of the breaking waves were measured photographically with a laser-induced fluorescence (LIF) method that employs a high-speed digital camera (Phantom V9, Vision Research) with a frame rate of 250 images per second. The camera was oriented to view the waves from the side with a look-down angle of about 5° from the horizontal. The camera was mounted on an instrument carriage that rides on oil-film bearings above the tank. The carriage is towed along the tank by a wire rope that is in turn driven by a servo motor. The same computer that controls the wave maker motion controls the carriage motion via a feedback loop employing a 7.6 m long position sensor. The starting time relative to the wave maker motion, acceleration, and final speed of the carriage were set by trial and error so that the field of view of the camera was centered on the wave crest (the highest water elevation) as it broke. The final carriage speed in the present study was $U = 1.23$ m/s. The wave crests were illuminated with a light sheet from an Argon-Ion laser operating at 7 W. The laser was mounted next to the tank, and a system of mirrors mounted to the tank was used to redirect the beam horizontally along the center plane of the tank at the height of the carriage. Mirrors mounted on the carriage and lenses mounted to the tank and the carriage were used to convert the beam into a vertical light sheet that translated along the tank with the carriage illuminating the breaking wave crest (see Figure 1). The light sheet was 1 mm thick at the mean water level. Fluorescein dye was mixed into the tank water and the dye fluoresced where the light sheet impinged on the water surface. A long-pass optical filter was placed in front of the camera lens to reject the specular reflections of laser light from the water surface while accepting the light from the fluorescing dye. With this illumination, the intersection of the light sheet and the water surface (wave profile) along the centerline of the tank could be seen in each image. The wave profiles were extracted from the digital images using gradient-based methods as described in detail in *Liu and Duncan* [2006].

2.3. Water Treatment and Surfactant Solutions

A similar water treatment procedure as described in *Liu and Duncan* [2006] was used in the present study. At the beginning of the experiment, the tank was filled with filtered tap water and hypochlorite was added at a concentration of 10 ppm to neutralize organic materials. Low winds were used to blow surfactants and floating dust particles to the end of the tank farthest from the wave maker where they were collected by a surface skimmer. The water from the skimmer went through a diatomaceous earth filter and then back into the wave tank at the end near the wave maker. Just before the wave-breaking experiments began, the free chlorine level in the tank was reduced to less than 3 ppm by the addition of an appropriate amount of hydrogen peroxide. A fluorescein dye was then mixed with the water for the LIF crest profile measurements. The reduction in chlorine level was necessary to preserve the dye. It is important to realize that, even with the above water-treatment procedures, these experiments were not performed with solutions of pure water

and Triton X-100. The water in the tank was not distilled and the dye and the surfactants added to the tank water probably contained other surfactants. Additional surfactants may have entered the tank by various paths. Periodically during the experiments, water samples were taken from near the breaker location using a carefully cleaned beaker and the ambient surface tension of the water sample was measured with a Whilhelmy plate tensiometer (ST9000, manufactured by NIMA Technology). The tank water samples were obtained when the wave maker and wind tunnel fans were off.

All the Triton X-100 solutions were made using a single tank of water over a period of 3 days. On the first day of the measurements, with zero bulk concentration of Triton X-100, the measured ambient surface tension of the water in the tank was 73 mN/m. The crest-profile histories of the breakers at various wind speeds were measured (the data are denoted CLEAN). After these measurements, 25 mL of Triton X-100 was added and mixed to the water. On the following day, the ambient surface tension was measured first and then a set of breaking wave profile measurements at various wind speeds was taken (data set TX25). This procedure (adding additional 76 mL of Triton X-100 at the end of the day and taking measurements on the following day) was repeated one more time to obtain another data set, denoted TX101. The bulk concentrations of Triton X-100 in the TX25 and TX101 solutions were 2.5 and 10.3 μmol L^{-1}. The ambient surface tensions of these two solutions were 58 and 45 mN/m, respectively. Our previous work [*Liu and Duncan*, 2006] and laboratory measurements with pure water and Triton X-100 by *Fainerman et al.* [2009] have shown that the surface-to-bulk-diffusion time constant is of the order of 100 s at these low concentrations of Triton X-100. Therefore, the surfactant can be considered as insoluble during the wave breaking time scale, which is about 1 s.

3. Results

3.1. The Effects of Light-Winds on Wave Breaking in Clean Water

Figure 3 shows two columns of four photographs of wave crests from the high-speed LIF movies of two waves crests breaking in clean water. In the left column of photographs (Figures 3a–3d) the wind speed is zero while in the right column of photographs (Figures 3e–3h), the wind speed is $U_0 = 2.3$ m/s. Figure 4 shows crest profile histories extracted from the movies of these two breaking events. As described in section 2, the profiles are measured (and shown here) in a reference frame moving with the crest of each breaker at $U = 1.23$ m/s (the horizontal speed of the highest water elevation). As can be seen from the profile histories, the wave breaking processes in clean water under these two wind conditions are qualitatively similar. In the case with no wind, Figure 4a and the left column of photographs in Figure 3, the breaking process starts with a bulge formation on the forward (left) face of the crest and capillary waves upstream of the leading edge of the bulge (called the toe). This bulge-capillary-wave pattern is similar to that reported in *Duncan et al.* [1999] and *Liu and Duncan* [2006, 2007]. A short time later, see Figure 3b, the toe begins to move rapidly down the wave's forward face. During this early upstream toe motion, a train of ripples appears between the toe and the crest, see Figure 3c, and this train of ripples is swept downstream. Later, the toe's speed relative to the crest decreases and the toe eventually reaches a maximum distance away from the wave crest before moving back toward the crest, see Figure 3d. The horizontal maximum distance (L_{ext}) of the toe away from the crest shown in Figure 4a is discussed in a later part of the present paper (see section 4.4). This breaking process is nearly the same for $0 \leq U_0 \leq 2.3$ m/s. With a wind speed of $U_0 = 2.3$ m/s (Figure 4b and the right column of Figure 3), which is found to be the minimum wind speed for the appearance of wind-generated waves in our tank, very weak wind waves are generated on the forward face of the wave crest. The amplitude of these wind waves is less than 0.5 mm. The wind waves have little effect on the formation of the bulge-capillary-waves pattern mentioned above (see Figure 3f). However, the ripples generated after the toe spills down the wave face for $U_0 = 2.3$ m/s are more violent than those in the case of no wind (compare Figures 3c and 3d with Figures 3g and 3h). The elapsed time between the bulge formation (Figure 3e) and the moment when the toe reaches the maximum distance from the crest (Figure 3h) is about 0.55 s for $U_0 = 2.3$ m/s and about 0.37 s (from Figures 3a–3d) for $U_0 = 0.0$.

When the wind speed is above $U_0 = 2.3$ m/s, the wind-generated waves become larger and have a dramatic effect on the breaking process of the mechanically generated waves. Figure 5a shows the crest-profile history of a mechanically generated spilling breaker in clean water with a wind speed of $U_0 = 3.0$ m/s, and

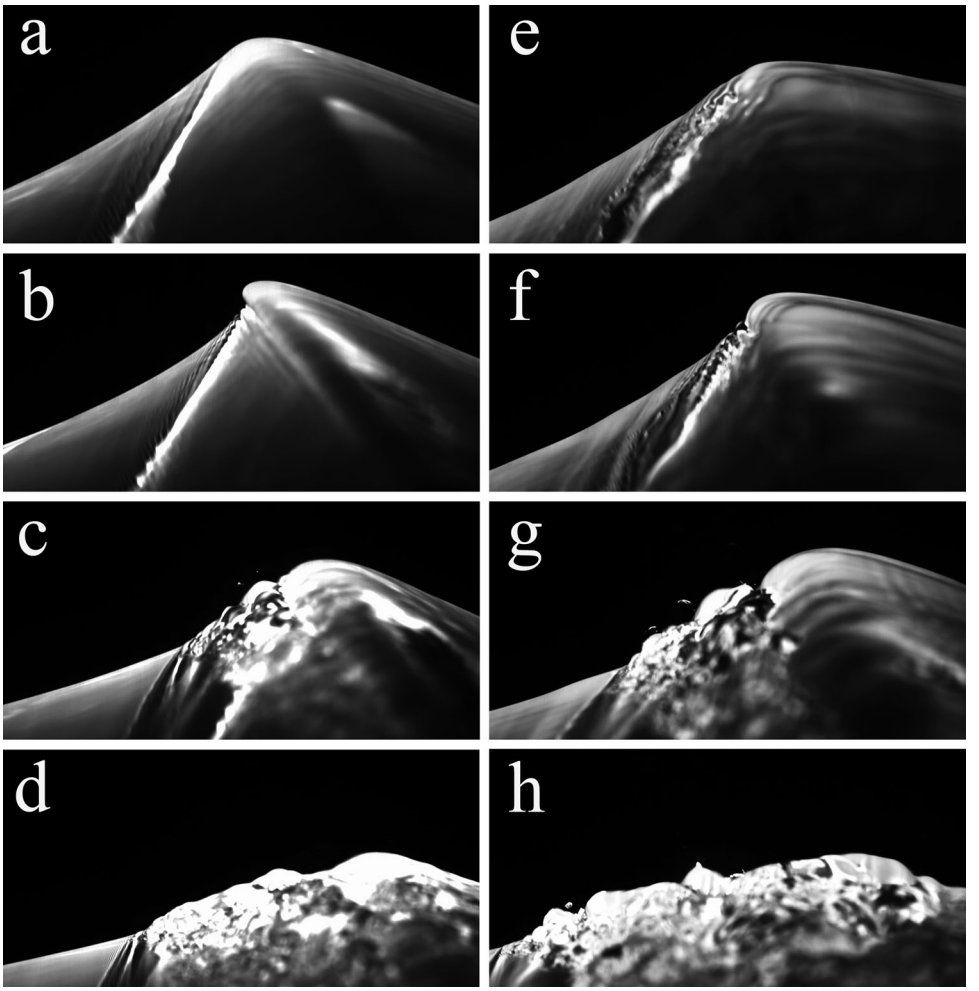

Figure 3. Images of wave crests in clean water (left column) without wind and (right column) with a wind speed of $U_0 = 2.3$ m/s. Each image shows a 13.2 × 6.6 cm section near the wave crest and the waves move from right to left. (a) $t_c = 0$ s and (e) $t_w = 0$ s, the bulges and toes are just beginning to form; (b) $t_c = 0.112$ s and (f) $t_w = 0.108$ s, the toe motions are about to start; (c) $t_c = 0.256$ s and (g) $t_w = 0.304$ s, ripples appear between the toe and crest; (d) $t_c = 0.372$ s and (h) $t_w = 0.548$ s, the toes spill down with the maximum distance away from the crest and the crests appear to be fully turbulent.

Figure 5b shows a profile history of wind waves at the same wind speed, but without the mechanically generated waves. The two profile histories in Figure 5 are shown in a reference frame moving with the speed of the crest of the mechanically generated wave, i.e., the same carriage speed was used in obtaining both profile histories. Lines connecting various features of the waves from profile to profile in Figure 5b are straight and parallel; their slopes indicate that the speed of the wind waves relative to the instrument carriage is 0.88 m/s from left to right, or 0.35 m/s from right to left in the laboratory reference frame. Also, analysis of the profiles indicates that the maximum amplitude of the wind waves is $a_w = 2$ mm and their average wavelength is $\lambda_w = 4$ cm. As can be seen from Figure 5a, in this reference frame, as the wind waves propagate from left to right toward the crest of the gravity wave, lines connecting wind wave features from one profile to another, steepen slightly indicating that they slow down relative to the crest. These waves also steepen. When a wind wave reaches the crest region of the mechanically generated wave it can trigger breaking or strongly affecting the spilling process. As can be seen from the profile history, when each wind wave reaches the toe of the breaking region, a large ripple is formed that then propagates downstream over the crest of the breaker. This interaction between the wind waves and the spilling process can be seen clearly in the three photographs in Figure 6 which were taken from the high-speed image sequence corresponding to Figure 5a. As shown in Figure 6a, a wind wave (marked by 1) appears on the forward face of the gravity wave while a weak breaking event is occurring downstream (to the right) of the wind wave at

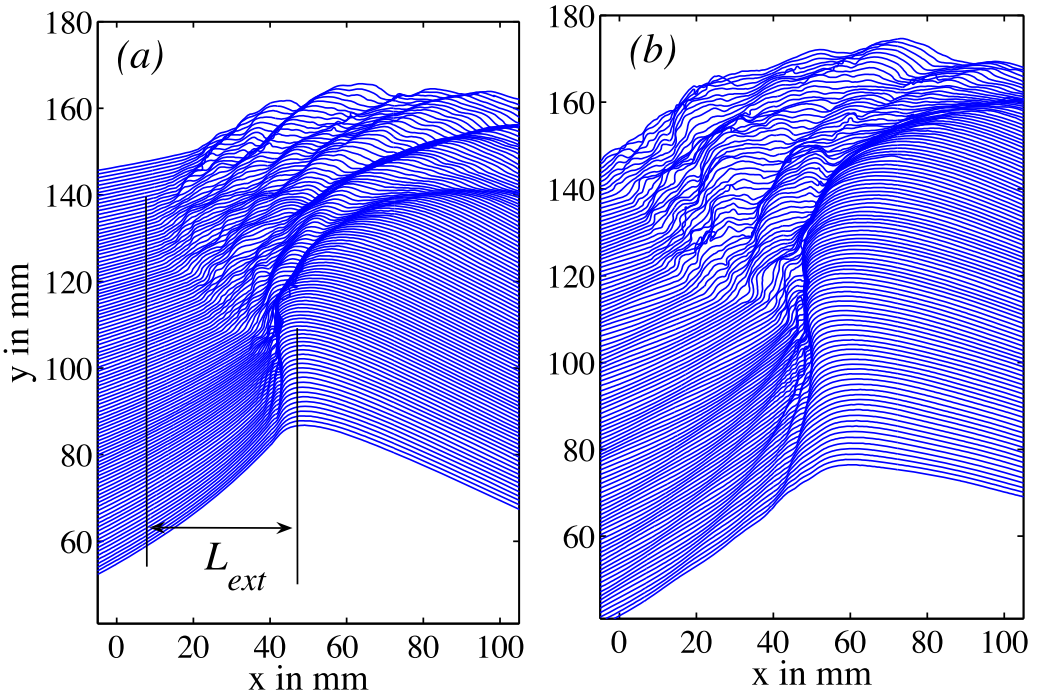

Figure 4. Two crest profile histories of spilling breaking waves in clean water under different wind conditions. (a), $U_0 = 0$ m/s (no wind) and (b) $U_0 = 2.3$ m/s. The waves and wind propagate from right to left. Each plot includes 110 profiles and each successive profile is plotted 1.0 mm above the previous profile for clarity. The profiles are shown in a reference frame fixed with respect to the wave crest. In this reference frame, the mean fluid motion is from left to right. The time between profiles is 0.4 ms.

the crest of the mechanically generated wave (the time of this photograph is designated as $t = 0$ ms). In Figure 6b, $t = 40$ ms, the wind wave moves relatively toward the breaking wave crest where the breaking water is tumbling forward. Later (Figure 6c, $t = 80$ ms), the crest of the wind wave collides with the forward

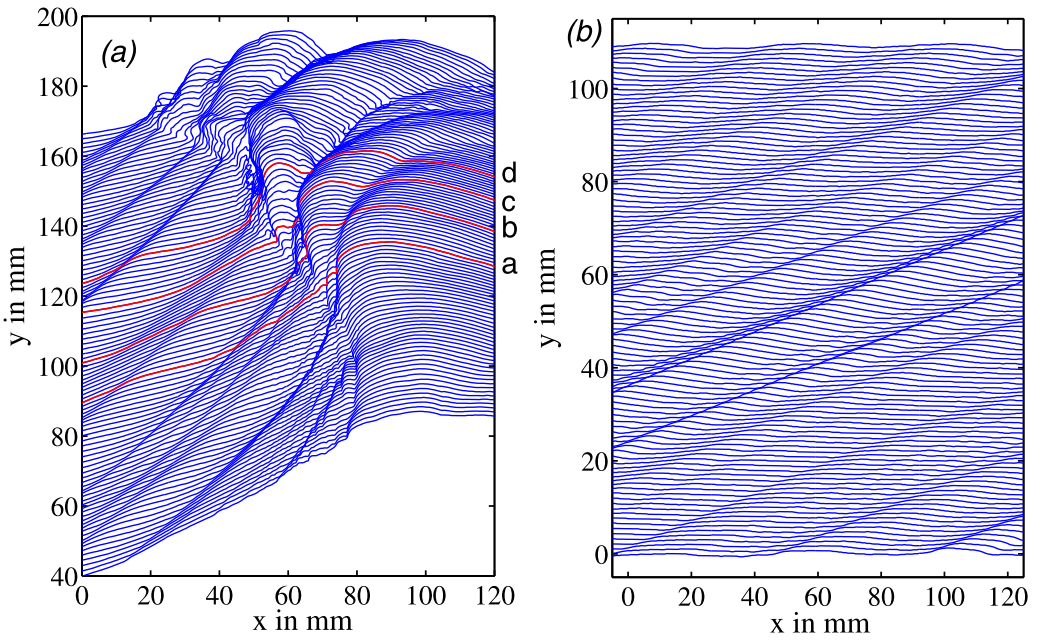

Figure 5. Profile histories of (a) a mechanically generated spilling breaking wave crest and (b) wind waves in clean water; the wind speed is $U_0 = 3.0$ m/s in both cases. Each plot includes 110 profiles and each successive profile is plotted 1.0 mm above the previous profile for clarity. All the waves propagate from right to left in the laboratory reference frame. The profiles are shown in the reference frame of the instrument carriage which is moving with the crest of the mechanically generated wave, at a speed of $U = 1.23$ m/s. In this reference frame, wind waves move from left to right because the carriage speed is greater than the phase speed of wind waves.

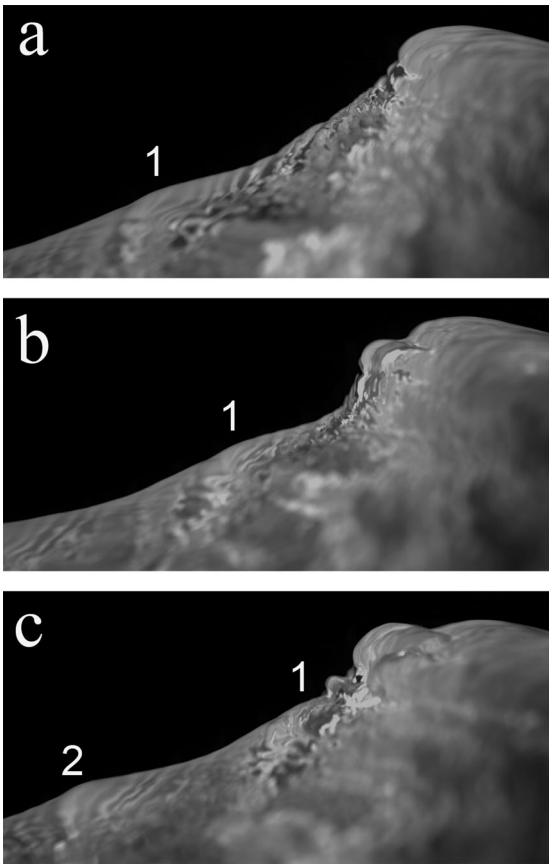

Figure 6. Photographs from a high-speed movie of the crest of a spilling breaker in clean water at a wind speed $U_0 = 3.0$ m/s. Each image shows a 13.2 × 6.6 cm section near the wave crest and the waves move from right to left. (a) A wind wave (marked by 1) appears on the forward face of the breaking wave crest. $t = 0$ ms. (b) The breaking water tumbles forward and the wind wave (label 1) approaches the breaking wave crest. $t = 40$ ms and (c) the crest of wind wave collides with the forward tumbling water, resulting in a big water splash (d in Figure 5). Another wind wave (label 2) appears in the image. $t = 80$ ms.

tumbling water from the breaking region, resulting in a violent splashing motion in the breaking region (d in Figure 5). Another wind wave (marked by 2) appears in the image window.

3.2. The Combined Effects of Light-Wind and Surfactants on Wave Breaking

Figure 7 shows three rows of two photographs of wave crests taken at the moment of incipient breaking in solutions TX25 (left column, Figures 7a, 7c, and 7e) and TX101 (right column, Figures 7b, 7d, and 7f) under three wind conditions (top row: $U_0 = 0.0$, middle row: $U_0 = 1.5$ m/s, and bottom row: $U_o = 2.3$ m/s). As can be seen from Figures 7a and 7b, in the presence of surfactants without wind, the breaking processes in both TX25 and TX101 still begins with the formation of a bulge-capillary-wave pattern on the forward face of the wave crest similar to that in the CLEAN case. However, in the presence of surfactants, the bulge shape is modified and the bulge size generally decreases with increasing surfactant concentration. Compared with the CLEAN case, all geometrical features of the capillary waves, including their number, amplitude, and length, become smaller, even at the lowest concentration of surfactants.

The wave crest shape at incipient breaking is significantly changed by light-wind. As can be seen from Figure 7c, the addition of wind with a speed of $U_0 = 1.5$ m/s to the wave in solution TX25 causes the bulge shape to become round, similar to that in clean water, see Figures 3b and 3f. Both the amplitude and length of the capillary waves become greater compared with those in the TX25 solution without wind, see Figure 7a. In contrast, the small bulge observed in solution TX101 with no wind, Figure 7b, becomes larger and flatter for $U_0 = 1.5$ m/s, Figure 7d. The capillary waves upstream of the toe in this surfactant solution are nearly the same under both wind conditions. It is interesting to note that the shapes of the bulge and capillary waves upstream of the toe in solution TX101 with $U_0 = 1.5$ m/s (Figure 7d) are very similar to those in solution TX25 without wind (Figure 7a). In fact, as shown in the comparison of the two measured wave crest profiles taken from images a and d and shown in Figure 8, they are nearly identical. Note that the surfactant bulk concentration of the TX101 solution is about 4 times higher than that of the TX25 solution. The similarity between these two wave crest profiles may indicate that the light-wind in TX101 reduces the surface concentration of surfactants by forcing the surface layer downwind faster than the surfactant is adsorbed onto the free surface from the bulk concentration in the water below. Thus, the surface dynamic properties of both solutions may be nearly the same. This hypothesis would indicate that the dynamical surface tension, for instance, of the TX101 solution under the wind condition of $U_0 = 1.5$ m/s is approximately the same as the measured ambient surface tension without wind in solution TX25, i.e., $\sigma_0 = 58$ mN/m.

As the wind speed increases ($U_0 = 2.3$ m/s), the average back-face slopes of the wave crest in both the TX25 and TX101 solutions decrease (Figures 7e and 7f). The number of the capillary waves in TX25 under this wind condition increases (Figure 7e). The number of capillary waves in TX101 with $U_0 = 2.3$ m/s (Figure 7f) does not change very much compared with that of the TX101 solution with $U_0 = 1.5$ m/s (Figure 7d). However, the locations of the toe and capillary waves relative to the wave crest in TX101 with $U_0 = 2.3$ m/s

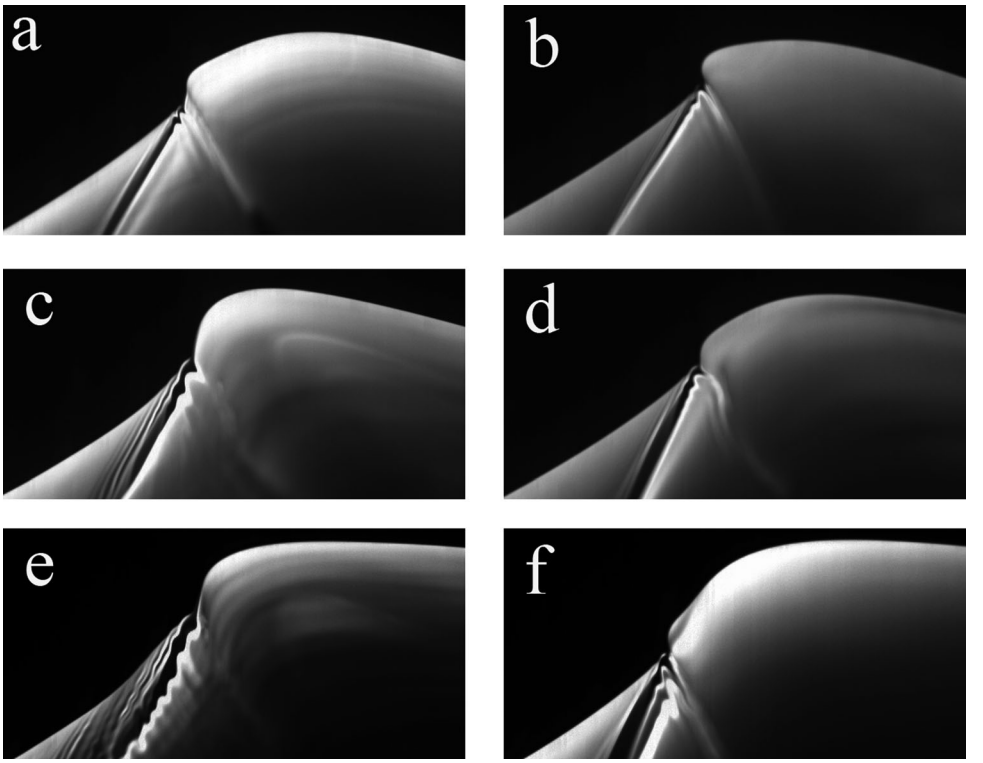

Figure 7. Images of wave crests at the moment of incipient breaking in solutions (left column) TX25 and(right column) TX101 under various wind conditions. Each image shows a 6.5 × 3.25 cm section near the wave crest and the waves move from right to left. (a and b) $U_0 = 0$ m/s (no wind); (c and d) $U_0 = 1.5$ m/s; (e and f) $U_0 = 2.3$ m/s.

become lower and the size of the bulge becomes larger compared to the case with $U_0 = 1.5$ m/s in the same solution.

Figure 9 shows four crest profile histories of spilling breakers in two surfactant solutions (TX25 and TX101) without wind (left column) and with the wind speed of $U_0 = 1.5$ m/s (right column). The profile history of the spilling breaker shown in Figure 9a (TX25 without wind) is similar to that shown in *Liu and Duncan* [2006, Figure 5]. Since the spatial resolution of the present data is 3 times higher than that in *Liu and Duncan* [2006], detailed features can be more easily observed in the present data set and are discussed in the following. As can be seen from Figure 9a, a little while after the formation of the bulge-capillary-wave pattern (the first wave profile at the bottom of the figure), the toe starts to move rapidly down the front face of the wave (the motion is marked by A in the figure). During this toe motion, small ripples with wavelength of about 4 mm (measured from tough to trough) form just downstream (to the right) of the toe. After this first set of ripples is generated, the

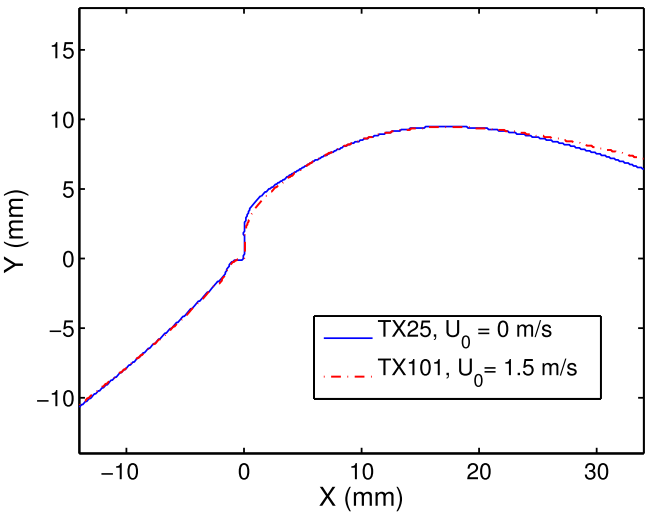

Figure 8. The comparison of wave crest profiles at instant that the toe starts to move in the TX25 solution without wind and the TX101 solution with $U_0 = 1.5$ m/s. The profiles are plotted in the coordinate aligned at the toe point to allow a better comparison.

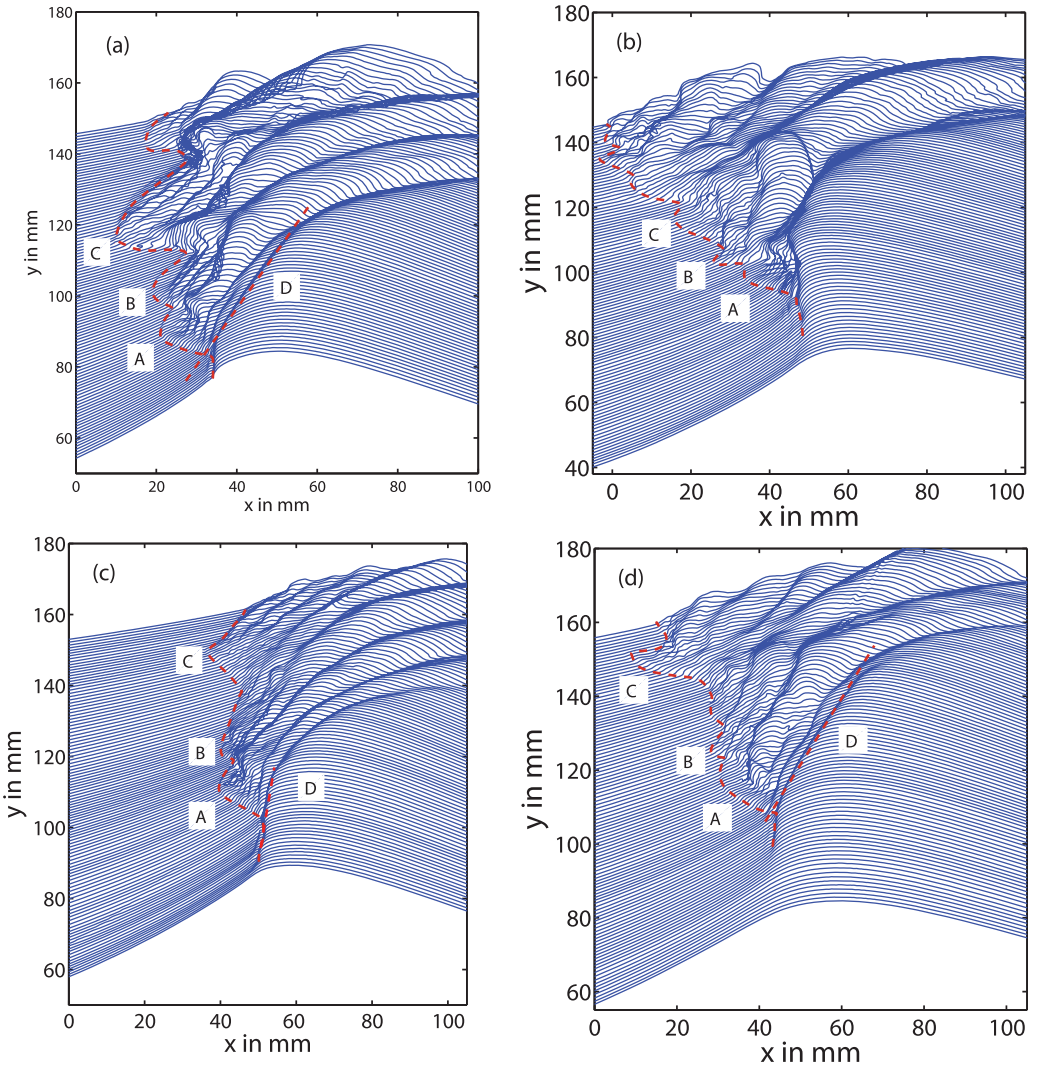

Figure 9. The crest profile histories of spilling breaking waves in two surfactant solutions (left column) without wind and (right column) at a wind speed $U_0 = 1.5$ m/s. (a) TX25, $U_0 = 0$ m/s (no wind); (b) TX25, $U_0 = 1.5$ m/s; (c) TX101, $U_0 = 0$ m/s (no wind); (d) TX101, $U_0 = 1.5$ m/s.

toe motion slows down. The ripples last a very short time (about 28 ms). When the toe begins to move down the wave face again (marked by B), a new train of larger ripples with wavelength of about 7 mm is generated just downstream of the toe. The ripples propagate with a speed a little less than that of the crest and disappear in about 48 ms. After this point, the toe again moves downslope (marked by C) and a third set of ripples with wavelength of about 12 mm appears. This set of ripples lasts a little longer time than those mentioned above and eventually disappear. It is interesting to note that following each set of ripples, large ripples that dominate the entire breaking region are generated. These ripples slow down and propagate backward over the crest in a manner similar to that of the clean-water case. Another feature shown in this figure is the straight trajectory of the trough of the first large ripple to the left of the crest in the beginning stage of the wave breaking (marked by D in the figure). This straight line with a positive slope indicates that the first trough has a constant velocity that is a little slower than the crest speed.

As more surfactants were added into the tank and the ambient surface tension was reduced to $\sigma_0 = 45$ mN/m (solution TX101), the aforementioned features of the wave breaking are dramatically changed (see Figure 9c). First, the speed of the toe decreases when it moves down the wave face during the second and third toe-motion cycles, i.e., after the first toe motion (label A), becoming closer to the wave crest speed (see labels B and C in the figure) and the ripples generated during each toe motion become weaker. This indicates qualitatively that the intensity of wave breaking decreases with increasing the surfactant concentration though, as was shown by *Liu and*

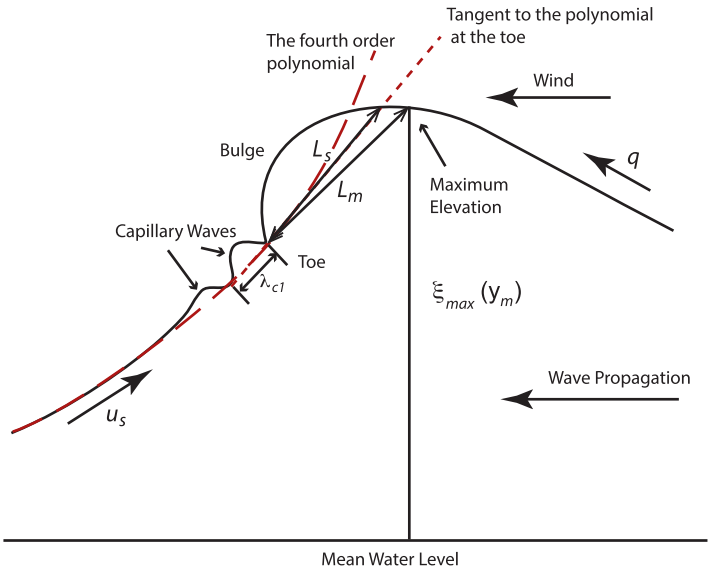

Figure 10. Schematic showing the nomenclature for the breaking wave profile.

Duncan [2006], if the Critical Micelle Concentration is reached the breaking intensity increases dramatically. Second, the trajectory of the trough of the first large ripple to the left of the crest has a finite radius of curvature at all points (D in the figure). The shape of the curved trajectory indicates that the velocity of the first trough decreases as the wave breaking continues.

The aforementioned features of the wave breaking shown in the profile history are changed when a light-wind ($U_0 = 1.5$ m/s) is applied on the water surface (Figures 9b and 9d). As can be seen from Figure 9b, the toe motion relative to the wave crest in TX25 with $U_0 = 1.5$ m/s becomes more complicated than that in the no-wind case. The toe makes at least four turns before it reaches the maximum distance away from the wave crest and a more violent ripple pattern is generated. The maximum distance of the toe away from the wave crest is greater than that in the same surfactant solution without wind. Similar results are also found in the solution TX101 (comparing Figures 9c and 9d). It has been shown in Figure 8 that the bulge-capillary-wave pattern formed at the beginning of the wave breaking in TX101 with $U_0 = 1.5$ m/s is very similar to that in TX25 without wind. A comparison of Figure 9d with Figure 9a shows that the profile histories in these two cases are quite similar (comparing the features marked by the A, B, C, and D in both figures). The detailed structures of the ripples generated between the toe and wave crest vary slightly between these two cases. The similarity of the crest-profiles histories between TX101 with $U_0 = 1.5$ m/s and TX25 without wind indicates that the initial geometry of the bulge-capillary-wave pattern may characterize the entire breaking process.

4. Discussion

Based on the above results, various aspects of the physics of the breaking process are discussed below in four subsections. Characteristics of the crest profile at the instant the toe starts to move down the wave face (the moment of incipient breaking) are discussed in sections 4.1–4.3. In these subsections, the effect of wind on the crest profiles in clean water and in water mixed with surfactant is discussed in sections 4.1 and 4.2, respectively, and a separate discussion of the effects of wind and surfactants on the length of the first capillary waves upstream of the toe is given in section 4.3. Finally, in section 4.4, the wave profile data are used to explore the effect of wind and surfactants on the size of the breaking zone of the waves, i.e., the maximum distance the toe moves away from the wave.

To quantitatively investigate the effects of wind and surfactants on the bulge-capillary-waves system, the complex shape of the crest profile must be represented by a small number of geometrical parameters. For this purpose, the parameters used in *Duncan et al.* [1999], *Liu and Duncan* [2006], and *Diorio et al.* [2009] are discussed herein. These parameters include the length of the first capillary wave upstream of the toe (λ_{c1}), the crest height (y_m) and two bulge lengths (L_m and L_s). The length L_m is the distance from the toe to the highest point on the wave profile, while the length L_s is the distance from the toe to the surface profile along the crest following the tangent to the smoothed water surface upstream of the toe. This smoothing was accomplished by fitting a fourth-order polynomial to the profile data in this region in order to eliminate the capillary waves, see Figure 10.

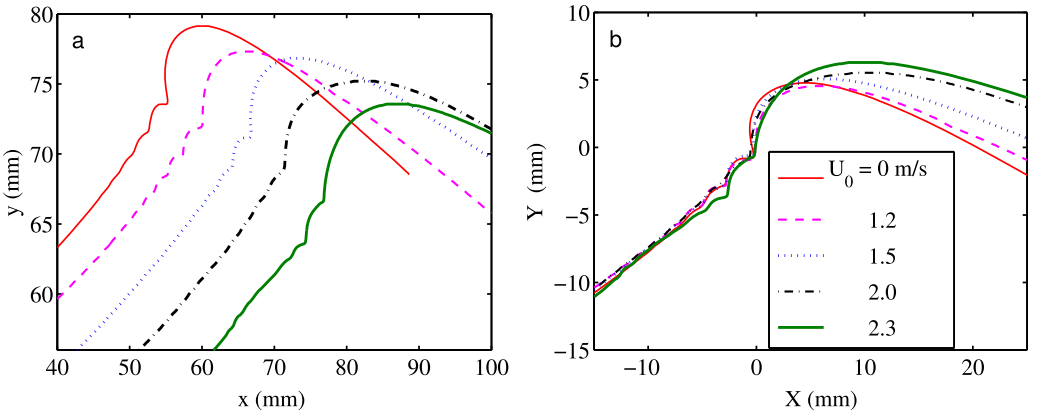

Figure 11. Crest profiles at the instant the waves start to break in clean water with various wind speeds. (a) In the coordinate relative to the mean water surface. (b) In the coordinate aligned at the toe point. The waves move from right to left.

4.1. The Crest Profile at the Moment of Incipient Breaking in Clean Water

Wave crest profiles taken from the images like those shown in Figures 3b and 3f in clean water (CLEAN) with various wind speeds are plotted in Figure 11a in a coordinate system with $y = 0$ at the mean water surface. For comparison purposes, the horizontal positions of these wave profiles were adjusted to bring them closer together in the plot, but without changing their relative order in position along the tank. (The actual distance from the left peak to the right peak is about 250 mm instead of 25 mm as depicted in the plot.) As can be seen from the figure, as the wind speed increases incipient breaking occurs closer to the wave maker (the wave propagates from right to left), indicating that the wave breaks earlier in time in the tank. Both the crest height and toe height decrease at the instant the wave starts to break. To allow better comparisons of the profile shapes, the crest profiles in Figure 11a are plotted again in Figure 11b, but with the origin for each profile shifted to the toe. As can be seen from Figure 11b, the slopes of the front faces of the waves and capillary waves upstream of the toe are nearly the same, indicating that this bulge-capillary-waves pattern is independent of the wind. However, the back face of the wave crest, where the surface curvature is almost zero, is markedly affected by the wind. As the wind speed increases, the slope of the back face of the wave crest decreases and the front-rear asymmetry of the wave crest increases.

The decrease of the toe height at the instant of incipient breaking with increasing wind speed is likely due to surface wind drift and may be explained qualitatively by the leaky-capillary-jump theory proposed by *Longuet-Higgins* [1996]. The theory applies to a steady wave without wind and postulates that the toe position is located at the place on the wave profile where the flow speed along the surface in the reference frame of the crest equals the minimum phase speed of capillary-gravity waves in still water, i.e.,

$$u_t = c_{\min} = 1.414\left(g'\frac{\sigma_0}{\rho}\right)^{1/4}, \tag{3}$$

where u_t is the local flow speed, σ_0 is the ambient surface tension, ρ is water density, and $g\prime = g\cos\alpha - \kappa u_t^2$ is the apparent local gravity, with α and κ being the local surface tilt angle and curvature, respectively. Since the mean slopes $(m = \tan\alpha)$ of the wave surfaces and the surface curvatures upstream of the toe at the point of incipient breaking are nearly the same for wind speeds less than or equal to 2.3 m/s, see Figure 11b, g' is the same and the flow speeds (u_t) near the toe have to be identical, according to equation (3). Using the experimental data obtained in our laboratory, *Diorio et al.* [2009] have shown that for the waves with wavelengths ranging from 10 to 120 cm, the flow speed at the toe position just prior to breaking correlates strongly with the wave surface slope at the toe. This surface slope is a function of the wave phase speed and the average growth rate of the wave amplitude before breaking starts. The values of u_t and α for the wave without wind used in the present paper are 38.2 cm/s and 56.3°, respectively. For a steady wave without wind, the magnitude of the surface flow velocity (u_s) in the reference frame of the wave crest increases along the front face of the wave as the vertical distance relative to the highest point of the wave crest increases [*Longuet-Higgins*, 1996]. As the wind blows over the water surface, a wind drift with a magnitude of q is generated in the opposite direction of u_s, as shown

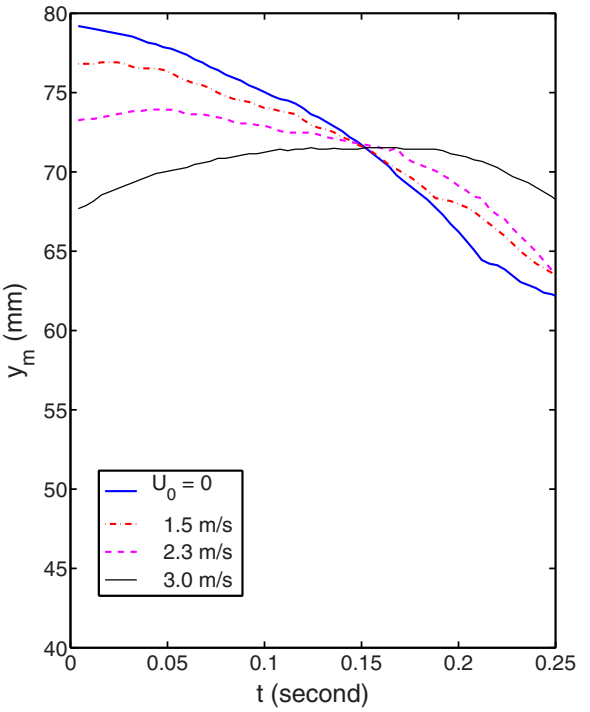

Figure 12. The evolutions of the highest point of the wave crest without wind ($U_0 = 0$) and with various wind speeds after the moment of incipient breaking ($t = 0$). The focusing point of the waves corresponds to the maximum crest height for each curve. For the case with $U_0 = 3.0$ m/s, wind waves with an average wavelength of 4 cm and amplitude of 2 mm were present in the tank whereas no visible wind waves were observed for the others.

in Figure 10 and the surface flow speed becomes $u_s - q$. In order to retain the flow speed $u_t = 38.2$ cm/s at the toe in the presence of wind, the underlying flow speed of the wave at the toe position must satisfy $u_s = u_t + q$, indicating that as q increases, u_s increases at the toe position, thus the toe height decreases. Also, the surface wind drift increases the steepness of the front face of the wave, thus the 56.3° surface tilt angle of the wave occurs earlier in time in the tank and the location of incipient breaking is shifted upstream (upwind). Since the wave has not reached the focusing point in the tank yet (see below), the crest height of the wave at the instant of incipient breaking decreases. This decrease of the crest height is consistent with the experimental result given by *Yao and Wu* [2005], who showed that a current with a positive shear, which is very similar to a wind-driven current on the water surface, reduces the steepness (the ratio of wave height to wavelength) of incipient breaking waves.

The upstream shift of the bulge-capillary-waves pattern should be distinguished from the downstream shift of the focusing point reported by *Kharif et al.* [2008] and others. The bulge-capillary-waves pattern is an indicator for the onset of spilling breakers. The experiments of *Kharif et al.* [2008] investigated the effects of strong wind on the formation of rogue waves. The wave elevations at various locations were measured by capacitive wave gauges. An amplification factor was used to describe the ratio of the maximal height between two consecutive crests and troughs in the wave group at various locations to that at a fetch of 1 m from the wavemaker. As the waves propagate in the tank, the amplification factor increases until its maximum at the focusing point and then decreases. The wind shifts the focusing point downstream and sustains high values of the amplification factor for a longer period of time after the focusing point. Since this amplification factor was not measured in the present study, Figure 12 shows the evolutions of the highest point of the wave crest without wind and with various wind speeds after the moment of incipient breaking ($t = 0$). As can be seen from the figure, the maximum wave amplitude (focusing point) of the wave without wind occurs at the same instant of the incipient breaking, i.e., $t = 0$. In the presence of wind, the maximum wave amplitude occurs after the moment of incipient breaking. The time difference between the incipient breaking and the maximum wave amplitude increases as the wind speed increases, indicating that the onset of wave breaking and the focusing point occur at different locations in the tank. In the presence of wind-generated waves (Case $U_0 = 3.0$ m/s in Figure 12), this time difference increases significantly.

The reduction of the crest height at the moment of incipient breaking with increasing wind speed may be used to calculate the surface wind drift. In a theory studying the effect of a surface wind drift on the incipient breaking condition in steady waves, *Banner and Phillips* [1974] predicted that the breaking wave amplitude (ξ_{max}) is given by

$$\xi_{max} = \frac{C^2}{2g}\left(1 - \frac{q}{C}\right)^2, \tag{4}$$

where C is the wave phase speed, g is the acceleration due to gravity, and q is the magnitude of the surface wind drift at the mean water level. In experiments with hydrofoil-produced waves in the presence of surface

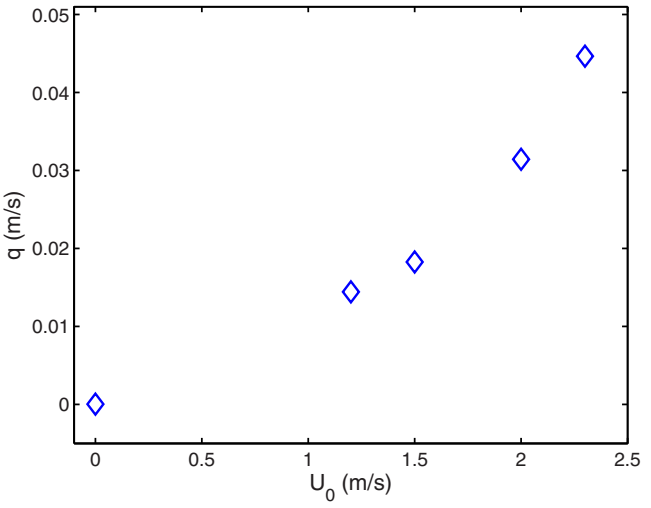

Figure 13. The wind drift (q) versus the wind speed U_0 in the tank.

wakes, *Miller et al.* [1999] found that the breaking condition has the same functional form as equation (4) but was reached when the flow speed at the crest was 50% of the wave speed. While the wave in the present study is clearly unsteady and to our knowledge, there is no theoretical work matching our experimental conditions, equation (4) is used here in an attempt to gain some understanding of the surface flow created by wind. In equation (4), the wave phase speed C is the carriage speed $U = 1.23$ m/s since the carriage moves with the same speed of the wave crest. Using the equation (4) and the wave amplitudes measured from Figure 11a yields the surface wind drift versus the wind speed U_0 and the result is shown in Figure 13. As can be seen from the figure, the surface wind drift q increases as the wind speed increases. The magnitude of q is a little less than 2% of the wind speed (U_0) while the wind friction velocity is about 2.16% of U_0 as shown in equation (2). Previous field and laboratory measurements by *Phillips and Banner* [1974], and *Wu* [1975, 1983] for a large range of wind speeds and fetches gave wind-induced surface drift currents a little larger than this, approximately 3.1–3.3% of the wind speed. In term of the aforementioned limitations in using equation (4) and rather different wind and fetch conditions, the present calculation of the surface wind drift is probably reasonable.

In an effort to explore the physical mechanisms that control the variations in bulge shape, plots of the lengths L_m and L_s at the instant the waves start to break versus the wind drift (q, as determined from the crest height measurements and theory) in CLEAN water are given in Figures 14a and 14b, respectively. The standard deviations of each point in the figure were obtained from three consecutive images (just before the moment the toe starts to move) in three repeated runs. The standard deviations in the measurements of both L_m and L_s increase with wind speed due primarily to the effect of the small-amplitude wind-generated ripples on the crest shape. This increase is more dramatic for the L_m measurements due primarily

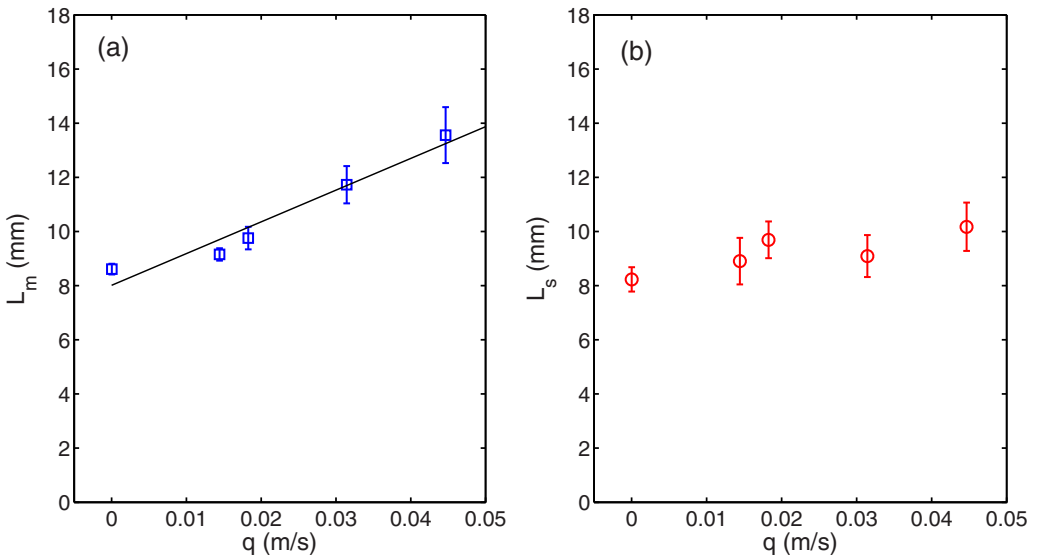

Figure 14. The variations of two bulge lengths (a) L_m and (b) L_s with the wind drift q in clean water. The solid line in Figure 14a is $L_m = sq + L_{m0}$ with $s = 0.117$ s and $L_{m0} = 8.0$ mm.

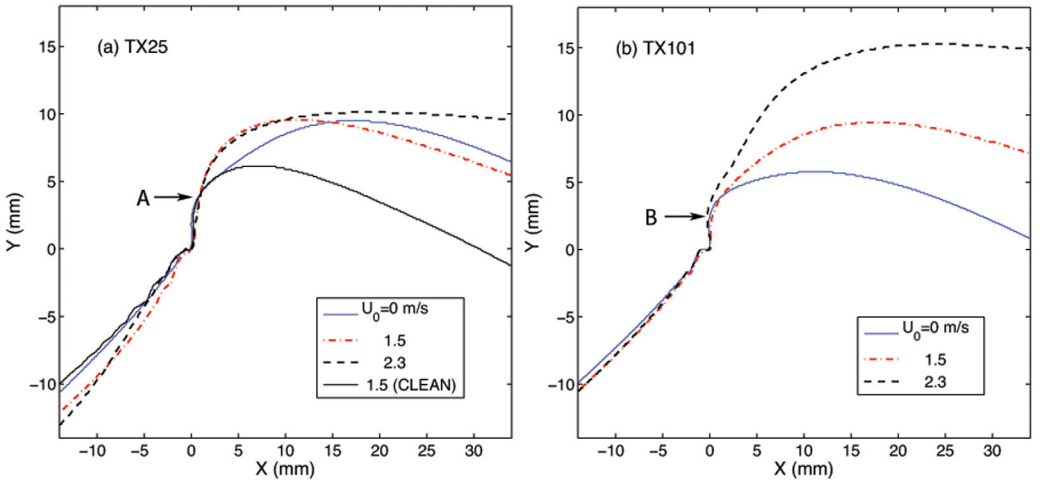

Figure 15. Crest profiles at instant the waves start to break in the surfactant solutions with various wind speeds. (a) TX25 and (b) TX101. The profiles are aligned at the toe point and the waves move from right to left.

to the effects of the ripples on the horizontal location of the height of the highest point on the profile. As can be seen from Figure 14a, the data follow a nearly linear relationship. A least squares fit of the equation $L_m = L_{m0} + s_0 q$ to the data yields the line with a slope $s_0 = 0.117$ s and intercept $L_{m0} = 8.0$ mm plotted in the figure. The value of L_{m0} is very close to the value of L_m observed under the no-wind condition. It is also noted that the slope s_0 is close to the formation time of the bulge, which was determined from the LIF movies to be in a range from 0.108 to 0.14 s and is not a function of the wind speed. (The variation of the formation time is due to the uncertainty in selecting the movie frame when the bulge is first visible.) This measured bulge formation time is consistent with the value $0.1/f_0$ reported by *Duncan et al.* [1999] for waves in clean water without wind. The reason for the linear relationship between L_m and q is not known; however, it is thought to be due to the downward shifting of the toe along the front face of the wave, as mentioned above.

As can be seen by comparing Figures 14b with Figure 14a, the length L_s increases more slowly with increasing q than does L_m (L_s increases from 8.5 mm at $q = 0$ to 10 mm at the highest q). In our previous work [*Diorio et al.*, 2009], it has been shown that at the moment of incipient breaking L_s depends primarily on the slope of the front face of the smoothed wave profile just upstream of the toe. In the present data, the slopes of the front face upstream of the toe in the CLEAN case with various wind speeds are nearly the same, thus the small change in L_s is consistent with *Diorio et al.* [2009]. Since L_s depends on the slope of the front face of the wave upstream of the toe (see its aforementioned definition) and intersects the wave crest profile substantially upstream of the peak of the profile, this parameter mainly describes the front face features of the wave while L_m, which depends strongly on the horizontal position of the peak of the profile, considers the entire shape of the wave crest. The different behaviors of L_m and L_s versus q are consistent with the fact that the effect of the wind on the back face of the wave crest is much stronger than that on the forward face and causes the slope of the back face to decrease while moving the peak backward horizontally relative to the horizontal position of the toe. The difference between the effects of the wind on both sides of breaking wave crest may be increased at high wind speeds due to air flow separation from the wave crest [*Reul et al.*, 1999; *Veron et al.*, 2007]. The weak effect of the wind on the forward face of the wave crest may be explained by the capillary-roller theory of *Longuet-Higgins* [1992]. In the theory, Longuet-Higgins has shown that the capillary-roller system is self-sustaining and the effect of the wind stress on the system is negligible compared to the capillary-wave stress. The energy of the system is supplied by the gravity wave.

4.2. The Crest Profile at the Moment of Incipient Breaking in the Triton X-100 Solutions

Figure 15 contains plots of the wave crest profiles for the two surfactant solutions, TX25 and TX101, with various wind speeds. These profiles were obtained from the images shown in Figure 7. The wave crest profiles in solution TX25 under three different wind conditions are given in Figure 15a while the crest profiles in solution TX101 under the same wind conditions are shown in Figure 15b. For comparison purposes, the

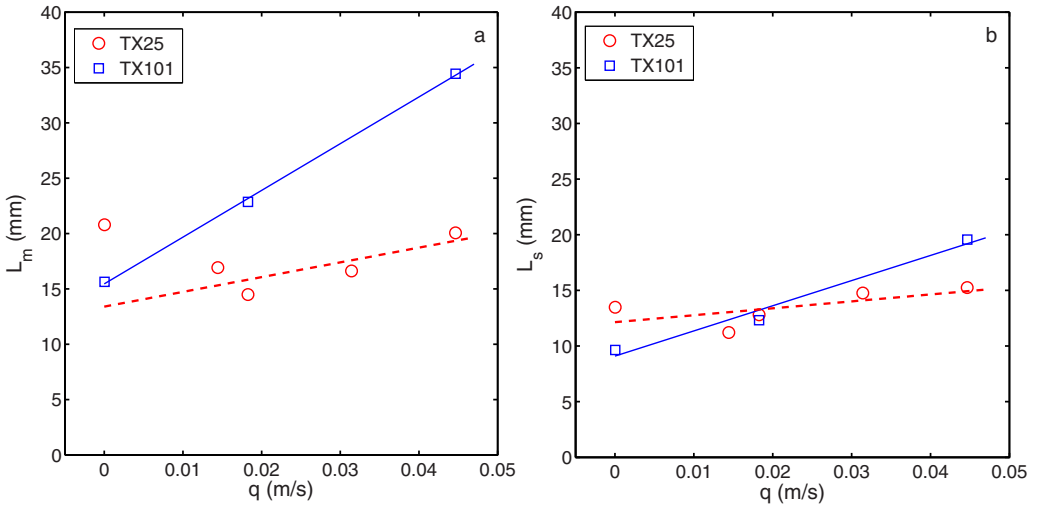

Figure 16. The lengths (a) L_m and (b) L_s versus the wind drift q in TX25 and TX101. The straight lines are the least squares fits to the data points for each solution.

wave crest profile in clean water at the wind speed $U_0 = 1.5$ m/s is also plotted in Figure 15a. As can be seen from the plots, the shapes of the profiles upstream of the point A in Figure 15a and point B in Figure 15b are quite similar in each plot (except for the length of the capillary waves, which are discussed in the following subsection), indicating that the mean surface slope upstream of the bulge, the toe, and the portion of the bulge in the vicinity of the toe are not strongly affected wind. Downstream of points A and B, the shapes of the wave crest change dramatically with the wind speed and the concentration of Triton X-100. In the TX25 solution, the flat bulge that occurs under the no-wind condition becomes round as the wind is applied while the vertical distances from the toe point to the maximum height of the wave crest remain nearly the same for all wind conditions. It should also be noted that this vertical distance is much greater in the TX25 cases than it is in the CLEAN case. In contrast to the behavior in the TX25 solution, in the TX101 solution, as the wind speed is increased, the bulge becomes flatter and the vertical distance from the toe point to the maximum elevation increases monotonically.

Figure 16 shows the bulge lengths L_m (a) and L_s (b) versus the wind drift speed (q, taken from Figure 13) in the TX25 and TX101 solutions. As can be seen in Figure 16a, the values of L_m for the four cases with nonzero wind drift follow a nearly linear relationship like the CLEAN case (Figure 14a). Using a least squares fitting of the equation $L_m = L_{m1} + s_1 q$ to this data yields $s_1 = 0.13$ s and $L_{m1} = 13.4$ mm. The corresponding bulge formation times are given in Table 1 and it can be seen that the three values for the nonzero q cases are consistent with the slope of the fitted line, in agreement with the CLEAN case discussed above. It is noted that for the case with $q = 0$, the L_m value is about twice as high as the value from the fitted line and the bulge formation time is about half of the values for nonzero q. In the TX101 case, using a least squares fitting of the equation $L_m = L_{m2} + s_2 q$ to the data of yields $s_2 = 0.42$ s and $L_{m2} = 15.4$ mm. Unlike the TX25 data, the measured values of the time interval of the bulge formation in TX101 (from 0.048 to 0.072 s, see Table 1) are much smaller than the slope of the line fitted to the L_m data.

It is difficult to explain the high value of L_m in the case of TX25 without wind, and the small values of the bulge formation time s in the case of TX25 without wind and s_2 in all three cases of the TX101 solution. However, it is thought that L_m is strongly influenced by other surface dynamic properties, in addition to the surface tension [*Liu and Duncan*, 2006]. In the presence of surfactants, a surfactant monolayer is formed on

Table 1. The Time Intervals From the First Visible Bulge to the Instant That the Toe Starts to Move Under Various Surfactant and Wind Conditions

	TX25	TX25	TX25	TX25	TX101	TX101	TX101
U_0 (m/s)	0	1.2	1.5	2.0	0	1.5	2.3
s (s)	0.06	0.116	0.13	0.112	0.048	0.06	0.072

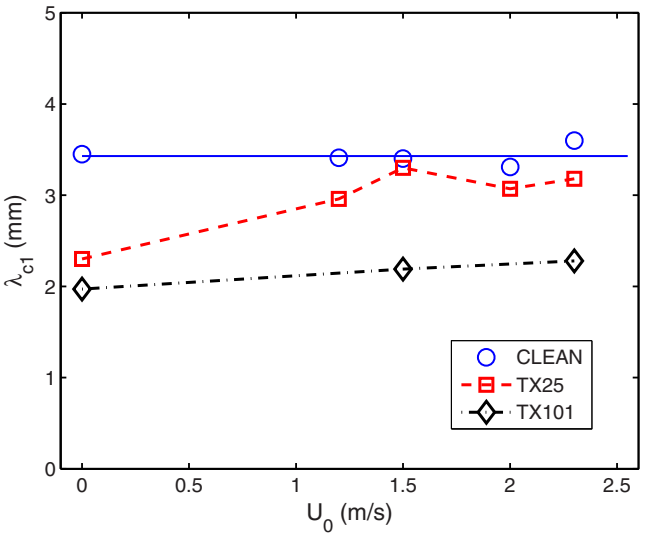

Figure 17. Lengths of the first capillary waves upstream of the toe (λ_c) versus the wind speed U_0 in clean water and two Triton X-100 solutions. The horizontal line is the average wavelength of the first capillary waves in CLEAN case (3.5 mm).

the water surface. This surfactant monolayer is a compressible surface film that lowers the surface tension and creates surface elasticity and also surface viscosity [see for example, *Edwards et al.*, 1991]. The surface elasticity supports longitudinal flow motion in the water surface [*Liu et al.*, 2007]. As the wave propagates in the tank, a high concentration of surfactants was found in the bulge-capillary region, as shown by the numerical simulation by *Ceniceros* [2003]. Thus, the surface tension in the bulge-capillary region is lower than that in the surrounding area, and surface tension gradients form. It is conjectured that surface tension gradients weaken the surface flow upstream of the toe while enhancing the surface flow on the back face near the wave crest in the reference frame of the wave crest. This results in a change of the shape of the wave crest and a relatively slow motion of the highest point of the crest profile in the laboratory reference frame. In addition, the unknown surface fluid longitudinal motion that is supported by the surface elasticity may affect the bulge length L_m. In the presence of wind, the surface dynamics of surfactant solutions and the shape of the wave crest profile are even more complex. Therefore, a further study is expected.

Figure 16b shows that the length L_s in the TX25 solution slightly increases linearly from approximately 13 to 15 mm with increasing surface wind drift, similar to that in the CLEAN case. However, the length L_s in the TX101 solution increases linearly at a substantially higher rate with increasing wind speed.

4.3. The First Capillary Wave and Dynamic Surface Tension

Figure 17 shows a plot of the length (λ_{c1}) of the first capillary wave upstream of the toe (at the moment of incipient breaking) versus the wind speed (U_0) in the CLEAN, TX25, and TX101 solutions. Each data point in the figure is the average from three or four separate experimental runs. As can be seen from the figure, the values of λ_{c1} for the CLEAN case are approximately the same (very close to their mean value of 3.5 mm) for all wind speeds, showing that the capillary wave system is not affected by wind. In the TX101 case, λ_{c1} increases as the wind speed increases. The increase of λ_{c1} with increasing wind speed is likely due to the reduction of surfactants on the water surface. In the presence of wind, the surfactants on the water surface are blown to the end of the tank, away from the location where the wave breaks. As the wind speed increases, the reduction rate of surfactants on the water surface increases. Meanwhile, surfactants from the bulk are adsorbed onto the free surface to compensate the reduction of surfactants due to the wind. However, the adsorption rate of surfactants onto the water surface is controlled by the bulk concentration of surfactants, which is the same for all wind conditions. Thus, the surface concentration of surfactants decreases as the wind speed increases, resulting in an increase of surface tension at the air-water interface [*Edwards et al.*, 1991]. Since the wind has minimal effects on the capillary wave and the wavelength of capillary waves is dominated by surface tension, the surface tension of surfactant solutions in the presence of wind may be determined by

$$\sigma_0 = \frac{\lambda_{c1}}{m}, \tag{5}$$

where $m = 0.043\ \mathrm{m^2\ N^{-1}}$ according to *Liu and Duncan* [2006].

Figure 17 also shows that λ_{c1} in the TX25 solution increases with increasing wind speed until $U_0 = 1.5$ m/s, but beyond this wind speed, λ_{c1} has nearly the same value as that in the CLEAN case. The behavior of λ_{c1} in the TX25 solution indicates a relatively clean water surface for a wind speed higher than 1.5 m/s. This clean water surface is likely caused by a higher wind-induced reduction rate of surfactants on the water surface than the absorption rate of surfactants onto the free surface from the bulk.

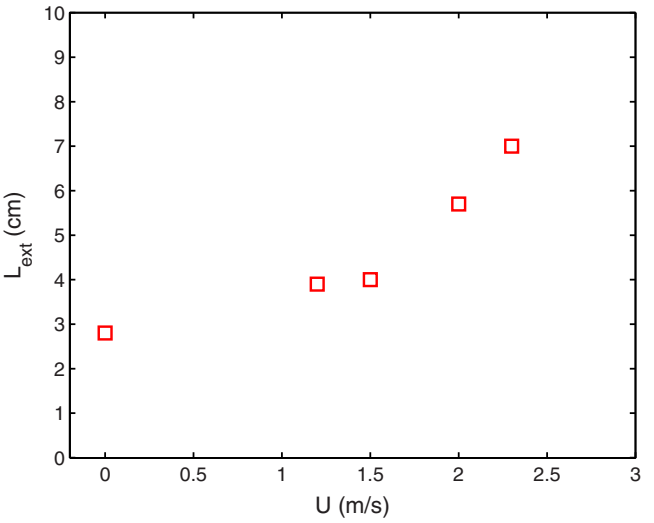

Figure 18. The maximum horizontal distance (L_{ext}) of the toe away from the wave crest versus the wind speed U_0 in the CLEAN water.

4.4. The Maximum Horizontal Distance of the Toe Away From the Wave Crest

Figure 18 shows the maximum horizontal distance (L_{ext}) of the toe away from the crest varying with the wind speed in the clean water. As can be seen from the figure, the distance L_{ext} increases as the wind speed increases in a nonlinear fashion. In general, this behavior indicates that the turbulence generated during the wave breaking at the wave crest is enhanced by the wind.

Figure 19 shows the ratio of the maximum distance of the toe away from the wave crest (L_{ext}) to the bulge length (L_m) at the moment of incipient breaking as a function of the wind speed in three solutions (CLEAN, TX25, and TX101). As can be seen from the figure, the data points are divided into two groups. The first group of data points in the upper half of the figure ($L_{ext}/L_m > 3$) is obtained from the all of the CLEAN water experiments and the TX25 experiments with high wind speeds, where the lengths of the first capillary waves upstream of the toe are nearly the same as that in clean water (see Figure 17), indicating that the local surface tension is close to that in clean water. The second group ($L_{ext}/L_m < 3$) is obtained from surfactant solutions where the value of λ_c is less than that in clean water (the low-wind-speed TX25 experiments and all of the TX101 experiments), indicating that the local surface tension is reduced (equation (5)). Both groups of data show that the ratio L_{ext}/L_m increases with increasing wind speed. However, the slope of the fitting line for the first group of data set is little greater than that in the second group. Also, the ratio L_{ext}/L_m in the first group is almost 2 times greater than that in the second group. It is likely that these differences coincide with the reduction of water surface tension.

Laboratory experiments performed by *Banner and Peirson* [1998] show that, prior to the formation of wind waves, the tangential viscous shear stress beneath wind-driven air-water interfaces contributes the entire wind stress. The data shown in Figure 19 were measured when no visible wind waves appeared in the tank. Thus, the increase of L_{ext}/L_m with increasing wind speed is likely an indication that the tangential stress induced by wind interacts with the turbulence generated during the wave breaking at the wave crest and transmits the atmospheric wind stress into the wave turbulence.

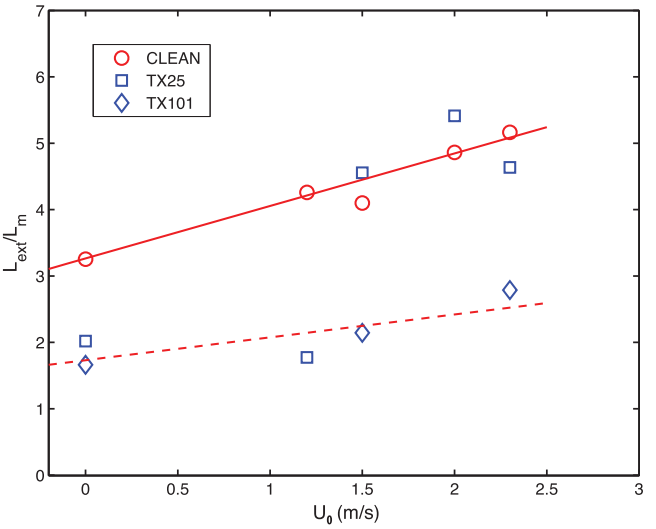

Figure 19. The ratio of L_{ext}/L_m versus the wind speed U_0 in CLEAN, TX25, and TX101 solutions. The straight lines are the least squares fits to each set of the data points.

5. Conclusions

The crest profiles of spilling breakers in the presence of light-wind and ambient surfactants were investigated experimentally. The waves were generated with a wave maker motion that produces a weak spilling breaker in clean water without wind. In clean water with a wind speed lower than the minimum wind speed of wind-generated waves, the breaking process described in

Duncan et al. [1999] changes quantitatively with the wind speed. The breaking process starts with a formation of a bulge on the forward face of the wave crest and the appearance of capillary waves upstream of the leading edge (toe) of the bulge. It is found that the capillary waves do not change with wind speed, but the length of the bulge (from the toe to the highest point of the wave crest) increases linearly with the surface wind drift. As the wind speed is above 3.0 m/s, wind waves were generated in the tank. These wind waves steepen up as they approach the front face of the crest of the mechanically generated waves and strongly affect the spilling process. In the presence of surfactants, the breaking process described in *Liu and Duncan* [2006] changes both qualitatively and quantitatively. At low concentration of surfactants, the flat bulge obtained in surfactant solution without wind become round as the wind speed increases in the tank. The amplitude of the capillary waves becomes larger. The wavelength of the capillary waves increases with the wind speed until the value similar to that in clean water is reached. At high concentration of surfactants but below the Critical Micelle Concentration, the small bulge observed in surfactant solution without wind becomes larger and flatter as the wind speed increases. The capillary waves change slightly with the wind. It is found that the length of the bulge in surfactant solutions increases linearly with the surface wind drift as well. After the flow in the region of the wave crest transitions to turbulence, the maximum horizontal distance of the toe away from the crest increases as the wind speed increases.

To better understand the dynamics of spilling breakers in the presence of wind and surfactants, several aspects of this flow require further investigation in both laboratory and the field. First, the spatial variations of the surface drift of the fluid flow before and after the moment of incipient breaking should be pursued in laboratory because the nonuniformity of surface fluid velocities along the wave crest profile may be a significant source of surface shear stress. *Peirson and Banner* [2003] have performed a laboratory study in which flow velocity measurements were made within a few hundred micrometers of the surface of microscale breaking wind waves, by using flow visualization and particle image velocimetry techniques. In the presence of surfactants, a surfactant monolayer is formed on the water surface. It would be very difficult to measure the surface drift within this monolayer for spilling breakers over a wide range of wavelengths and breaking intensities. Second, because surfactants have strong effects on surface-tension-dominated spilling breakers, the surface dynamics of surfactants in the presence of wave breaking are clearly important, but have received little attention. Third, details of wind forcing (pressure and shear stress) on the top of the bulge-capillary-waves pattern should be further investigated [*Banner and Song*, 2002]. Finally, where possible, detailed experiments should be extended to spilling breakers with high winds, in which the breaking of large waves will be drastically affected by wind-generated waves (see section 3).

The effects of wind and surfactants on air-water heat and gas transfer have been investigated by *Zappa et al.* [2004], while the effects of surface tension on wave dissipation have been studied experimentally by *Stagonas et al.* [2011]. To apply the present laboratory results to the field, more realistic ocean conditions should be considered, including, for example, three-dimensional short-crest waves on various wind, current, and surfactants backgrounds. The effects of wave directionality on breaking wave energy loss have been highlighted by *Wu and Nepf* [2002]. A number of experiments investigating the effects of various currents on the breaking of mechanically generated waves have been given by *Yao and Wu* [2004, 2005] and *Wu and Yao* [2004]. Since the temperature and salinity of water have little effect on surface tension, it is unlikely that those factors are important to the formation of the bulge-capillary-waves pattern of spilling breakers. However, both of these factors have significant effects on the population of the bubbles generated by wave breaking [*Callaghan et al.*, 2014], resulting in drastic effects on the wave turbulence. Further examination on this issue is highly desired.

Acknowledgments
The work is supported by the Division of Ocean Sciences, National Science Foundation, under award 092107 and award 1061998. The author would like to thank James H. Duncan for numerous suggestions and reviewing this manuscript and Dan Wang for her assistance with taking the measurements and processing the images.

References

Banner, M. L., and W. L. Peirson (1998), Tangential stress beneath wind-driven air-water interfaces, *J. Fluid Mech.*, *364*, 115–145.
Banner, M. L., and O. M. Phillips (1974), On the incipient breaking of small scale waves, *J. Fluid Mech.*, *65*, 647–656.
Banner, M. L., and J. Song (2002), On determining the onset and strength of breaking for deep water waves. Part II: Influence of wind forcing and surface shear, *J. Phys. Oceanogr.*, *32*, 2559–2570.
Callaghan, A. H., M. D. Stokes, and G. B. Deane (2014), The effect of water temperature on air entrainment, bubble plumes, and surface foam in a laboratory breaking-wave analog, *J. Geophys. Res. Oceans*, *119*, 7463–7482, doi:10.1002/2014JC010351.
Ceniceros, H. D. (2003), The effects of surfactants on the formation and evolution of capillary waves, *Phys. Fluids*, *15*, 245–256.
Ceniceros, H. D., and T. Y. Hou (1999), Dynamic generation of capillary waves, *Phys. Fluids*, *11*(5), 1032–1050.
Coakley, D. B. (1997), Surface shape of laboratory-generated steady breaking waves, PhD thesis, Univ. of Md., College Park.
Dabiri, D., and M. Gharib (1997), Experimental investigation of the vorticity generation within a spilling water wave, *J. Fluid Mech.*, *330*, 113–139.

Diorio, J. D., X. Liu, and J. H. Duncan (2009), An experimental investigation of incipient spilling breakers, *J. Fluid Mech.*, *633*, 271–283.
Douglass, S. L. (1990), Influence of wind on breaking waves, *J. Waterw. Port Coastal Ocean Eng.*, *116*, 651–663.
Duncan, J. H. (2001), Spilling breakers, *Annu. Rev. Fluid Mech.*, *33*, 519–547.
Duncan, J. H., H. Qiao, H. Behres, and J. Kimmel (1994a), The formation of a spilling breaker, *Phys. Fluids*, *6*(8), 2558–2560.
Duncan, J. H., V. Philomin, H. Qiao, and J. Kimmel (1994b), The formation of a spilling breaker, *Phys. Fluids*, *6*, S2.
Duncan, J. H., H. Qiao, V. Philomin, and A. Wenz (1999), Gentle spilling breakers: Crest profile evolution, *J. Fluid Mech.*, *379*, 191–222.
Ebuchi, N., H. Wawamura, and A. Toba (1987), Fine structure of laboratory wind-wave surfaces studies using an optical method, *Boundary Layer Meteorol.*, *39*, 133–151.
Edwards, D. A., H. Brenner, and D. T. Wasan (1991), *Interfacial Transport Processes and Rheology*, Butterworth-Heinemann, Boston.
Fainerman, V. B., S. V. Lylyk, E. V. Aksenenko, L. Liggieri, A. V. Makievski, J. T. Petkov, J. Yorke, and R. Miller (2009), Adsorption layer characteristics of Triton surfactants. Part 2. Dynamic surface tension and adsorption, *Colloids Surf. A*, *334*, 8–15.
Fedorov, A. V., W. K. Melville, and A. Rozenberg (1998), An experimental and numerical study of parasitic capillary waves, *Phys. Fluids*, *10*(6), 1315–1323.
Kharif, C., J.-P. Giovanangeli, J. Touboul, L. Grare, and E. Pelinovsky (2008), Influence of wind on extreme wave events: Experimental and numerical approaches, *J. Fluid Mech.*, *594*, 209–247.
King, D. M., and C. J. Baker (1996), Changes to wave parameters in the surf zone due to wind effects, *J. Hydraul. Res.*, *34*, 55–76.
Lin, J. C., and D. Rockwell (1994), Instantaneous structure of a breaking waves, *Phys. Fluids*, *6*, 2877–2879.
Lin, J. C., and D. Rockwell (1995), Evolution of a quasi-steady breaking waves, *J. Fluid Mech.*, *302*, 29–44.
Liu, X., and J. H. Duncan (2003), The effects of surfactants on spilling breaking waves, *Nature*, *421*, 520–523.
Liu, X., and J. H. Duncan (2006), An experimental study of surfactant effects on spilling breakers, *J. Fluid Mech.*, *567*, 433–455.
Liu, X., and J. H. Duncan (2007), Weakly breaking waves in the presence of surfactant micelles, *Phys. Rev. E*, *76*, 061201, doi:10.1103/PhysRevE.76.061201.
Liu, X., J. H. Duncan, G. M. Korenowski, and J. S. Kelly (2007), A laboratory study of longitudinal waves in surfactant films in a water wave tank, *J. Geophys. Res.*, *112*, C06005, doi:10.1029/2006JC003867.
Longuet-Higgins, M. S. (1974), Breaking waves in deep or shallow water, in *Tenth Symposium on Naval Hydrodynamics*, pp. 597–605, Off. of Nav. Res., Arlington, Va.
Longuet-Higgins, M. S. (1992), Capillary rollers and bores, *J. Fluid Mech.*, *240*, 659–679.
Longuet-Higgins, M. S. (1994), Shear instability in spilling breakers, *Proc. R. Soc. A*, *446*, 399–409.
Longuet-Higgins, M. S. (1996), Capillary jumps on deep water, *J. Phys. Oceanogr.*, *96*, 1957–1965.
Longuet-Higgins, M. S. (1997), Progress toward understanding how wave break, in *Twenty-First Symposium on Naval Hydrodynamics*, pp. 7–28, National Academies Press, Washington, D. C.
Longuet-Higgins, M. S., and D. G. Dommermuth (1997), Crest instabilities of gravities waves. Part 3. Nonlinear development and breaking, *J. Fluid Mech.*, *336*, 33–50.
Miller, M., T. Nennstiel, J. H. Duncan, A. A. Dimas, and S. Prostler (1999), Incipient breaking of steady waves in the presence of surface wakes, *J. Fluid Mech.*, *383*, 285–305.
Okuda, K. (1982), Internal flow structure of short wind waves. Part I. On the internal vorticity structure, *J. Oceanogr. Soc. Jpn.*, *38*, 28–42.
Okuda, K., S. Kawai, and Y. Toba (1977), Measurement of skin friction distribution along the surface of wind waves, *J. Oceanogr. Soc. Jpn.*, *33*, 190–198.
Peirson, W., and M. L. Banner (2003), Aqueous surface layer flows induced by microscale breaking wind waves, *J. Fluid Mech.*, *479*, 1–38.
Phillips, O. M., and M. L. Banner (1974), Wave breaking in the presence of wind drift and swell, *J. Fluid Mech.*, *66*, 625–640.
Qiao, H., and J. H. Duncan (2001), Gentle spilling breakers: Crest flow-field evolution, *J. Fluid Mech.*, *439*, 57–85.
Rapp, R., and W. K. Melville (1990), Laboratory measurements of deep water breaking waves, *Philos. Trans. R. Soc. London A*, *331*, 735–800.
Reul, N., H. Branger, and J.-P. Giovanangeli (1999), Air flow separation over unsteady breaking waves, *Phys. Fluids*, *11*(7), 1959–1961.
Siddiqui, M. H. K., and M. Loewen (2007), Characteristics of the wind drift layer and microscale breaking waves, *J. Fluid Mech.*, *573*, 417–456.
Stagonas, D., D. Warbrick, G. Muller, and D. Magagna (2011), Surface tension effects on energy dissipation by small scale, experimental breaking waves, *Coastal Eng.*, *58*(9), 826–836.
Tsai, W.-T., and L.-P. Hung (2007), Three-dimensional modeling of small-scale processes in the upper boundary layer bounded by a dynamic ocean surface, *J. Geophys. Res.*, *112*, C02019, doi:10.1029/2006JC003686.
Tulin, M. P. (1996), Breaking of ocean waves and downshifting, in *Waves and Nonlinear Processes in Hydrodynamics*, edited by J. Grue et al., pp. 177–190, Kluwer, Dordrecht, Netherlands.
Uz, B. M., M. A. Donelan, T. Hara, and E. J. Bock (2002), Laboratory studies of wind stress over surface waves, *Boundary Layer Meteorol.*, *102*(2), 301–331.
Veron, F., G. Saxena, and S. K. Misra (2007), Measurements of the viscous tangential stress in the airflow above wind waves, *Geophys. Res. Lett.*, *34*, L19603, doi:10.1029/2007GL031242.
Wu, C. H., and H. Nepf (2002), Breaking criteria and energy losses for three-dimensional wave breaking, *J. Geophys. Res.*, *107*(C10), 3177, doi:10.1029/2001JC001077.
Wu, C. H. and A. Yao (2004), Laboratory measurements of limiting freak waves on currents, *J. Geophys. Res.*, *109*, C12002, doi:10.1029/2004JC002612.
Wu, J. (1975), Wind-induced drift currents, *J. Fluid Mech.*, *68*, 49–70.
Wu, J. (1983), Sea-surface drift currents induced by wind and waves, *J. Phys. Oceanogr.*, *13*, 1441–1451.
Yang, D., and L. Shen (2010), Direct-simulation-based study of turbulent flow over various waving boundaries, *J. Fluid Mech.*, *650*, 131–180.
Yao, Y., P. Wang, and M. P. Tulin (1996), Surface tension effects on breaking waves LONGTANK simulation, *Tech. Rep. 95-132*, Univ. of Calif., Santa Barbara.
Yao, A. and C. H. Wu (2004), Energy dissipation of unsteady wave breaking on currents, *J. Phys. Oceanogr.*, *34*, 2288–2304.
Yao, A. and C. H. Wu (2005), Incipient breaking of unsteady waves on sheared currents, *Phys. Fluids*, *17*, 082104, doi:10.1063/1.2000276.
Zappa, C. J., W. E. Asher, A. T. Jessup, K. Klinke, and S. R. Long (2004), Microbreaking and the enhancement of air-water transfer velocity, *J. Geophys. Res.*, *109*, C08S16, doi:10.1029/2003JC001897.